Coupled Discrete Element-Lattice Boltzmann simulations of settling behaviours of irregularly shaped particles

Pei Zhang,[1] S.A. Galindo-Torres,[2] Hongwu Tang,[1,*] Guangqiu Jin,[1] A. Scheuermann,[2] and Ling Li[2]

[1] *State Key Laboratory of Hydrology-Water Resources and Hydraulic Engineering, Hohai University, Nanjing, China*
[2] *School of Civil Engineering, University of Queensland, Queensland, Australia*

We investigated the settling dynamics of irregularly shaped particles in a still fluid under a wide range of conditions with Reynolds numbers (Re) varying between 1 and 2000, sphericity (ϕ) and circularity (c) both greater than 0.5, and Corey factor (CSF) less than 1. To simulate the particle settling process, a coupled Discrete Element-Lattice Boltzmann model combined with a turbulence module was adopted. This model was first validated using experimental data for particles of spherical and cubic shapes. For irregularly shaped particles, two different types of settling behaviours were observed prior to particles reaching a steady state: 'accelerating' and 'accelerating-decelerating', which could be distinguished by a critical CSF value of approximately 0.7. The settling dynamics were analysed with a focus on the projected areas and angular velocities of particles. It was found that a minor change of the starting projected area, an indicator of the initial particle orientation, would not strongly affect the settling velocity for low Re. Periodic oscillations developed for all simulated particles when $Re > 100$. The amplitude of these oscillations increased with Re. However, the periods were not sensitive to Re. The critical Re that defined the transition between the 'steady' and 'periodically oscillating' behaviours depended on the inertia tensor. In particular, the maximum eigenvalue of the inertia tensor played a major role in signalling this transition in comparison to the intermediate and minimum eigenvalues.

I. INTRODUCTION

The behaviour of solid particles in fluids is frequently encountered in both natural and industrial processes. Examples include sediment transport in rivers and lakes, suspension of fine particles in the atmosphere, particle mixing in a fluidized-bed reactor widely used in the chemical industry, and movement of activated sludge in settling and separating tanks. As a basic form of particle motion, settling has attracted interests of many researchers and has been studied experimentally [1–15] and numerically [16–21]. However, most previous investigations were based on particles of regular shapes such as spheres, cubes and ellipses [1, 16]. The simple particle geometries assumed in these studies are in contrast with complex irregular shapes that are commonly found in natural sediments and particles used in industrial processes. The irregular particle shapes are likely to affect significantly the motion of particles [2, 8].

As the simplest case, the settling of a sphere in a still fluid has been widely investigated. Two dimensionless numbers are used for quantifying the settling dynamics: the particle Reynolds number Re and the drag coefficient C_D. With the sphere's diameter d_n selected as the characteristic length and the terminal settling velocity u_p as the characteristic velocity, Re is defined as follows:

$$Re = \frac{u_p d_n}{\nu}. \tag{1}$$

The drag coefficient C_D indicates the magnitude of the drag force and is given by:

$$C_D = \frac{4dg(\rho_s - \rho_f)}{3\rho_f u_p^2}. \tag{2}$$

In Eqs. (1) and (2), ν is the kinematic viscosity of the fluid; ρ_s and ρ_f are the density of the solid sphere and the fluid, respectively; and g is the magnitude of the gravitational acceleration. Therefore, C_D is a function of Re. The drag force experienced by the particle can be written as:

$$F_D = C_D A_p \frac{\rho_f u_p^2}{2}, \tag{3}$$

where A_p is the projected area of the particle normal to the vertical axis in the settling direction.

The first theoretical solution for a sphere settling in a viscous fluid was derived by Stokes: $C_D = 24/Re$, with the limit of $Re \ll 1$ (also known as Stokes' regime) where the inertial force is negligible compared to the viscous force [22]. In the range of $2000 < Re < 30000$ (Newton's regime), C_D for spheres is approximately a constant around 0.45. Under the condition of a moderate Reynolds number between Stokes and Newton's regimes, both inertial and viscous forces are important and many empirical formulas for C_D in terms of Re have been proposed based on data obtained by settling experiments (see reviews by Clift et al. [3] and Khan [4]).

For non-spherical particles, C_D is generally higher than that for spheres at the same Re. Various corrections of the original Stokes formula have been proposed for well-defined regular particle shapes in Stokes' regime. For instance, corrections for spheroids and ellipsoids were given by Clift et al [3] and White [5], and for cube and octahedron by Leith [6] and Ganser [7]. The basic idea is

* hwtang@hhu.edu.cn

to introduce an additional term f_{shape}, which expresses essentially the ratio of drag coefficient for a particle of a non-spherical shape to that for a volume-equivalent sphere. f_{shape} is only related to shape factors. Similarly, corrections in Newton's regime have been proposed by Pettyjohn and Christiansen [10] and Stringham and Clarke et al [9]. At a moderate Reynolds number, Stokes' correction and Newton's correction are combined to predict the drag coefficient as reported by Ganser [7] and Cheng [11]. More corrections to account for the particle shape effects on the settling dynamics can be found in the review by Loth [8].

By using a shape factor based on sphericity (details in Sec. III), Haider [2] derived generalized drag coefficient and terminal velocity formulas for the range of $0.1 < Re < 100000$ based on data for particle shapes of disk, cube octahedron, octahedron and tetrahedron. It is important to remark that Haider's formulas are limited in the range of sphericity from 0.5 to 1, and for fairly isotropic particle shapes. Further improvement was made by Tran-Cong et al. [1] by measuring the drag coefficients and developing an empirical correction for six different geometrical shapes, which were created by ordered assemblies of several identical smooth glass spheres glued together. It should be pointed out that when Re exceeds 100, particles may develop of [13–15, 19] periodically oscillating and even chaotic behaviours, which hinder the applicability of these formulas.

Over recent years, direct simulations have become a widely used approach for investigating the interactions of solid particles and fluid. Ladd [23] developed a computational method for spheres settling in a viscous fluid by assuming particles as 'shells'. Cate et al. [12] reported a good agreement between simulation results given by Ladd's method and experimental data under conditions of relatively low Reynolds numbers with the wall boundary effect also considered. Beetstra et al. [18] preformed the simulation for clusters of spheres as used in Tran-Cong's experiment and found the dependence of the drag coefficient on the inter-particle distance. Hölzer and Sommerfeld [16] indicated that the drag coefficient is also related to the angle of incidence for non-spherical particles based on a three-dimensional simulation. A coupled Discrete Element-Lattice Boltzmann method was developed by Cook et al. [24] and Feng and Michaelides [20] with the Lattice Boltzmann Method (LBM) simulating the fluid and the Discrete Element Method (DEM) [25] simulating solid particles. So far, most research has been focused on the sphere or other regularly shaped particles. Irregularly shaped particles, if considered, were approximated as clusters of spheres, which do not represent fully natural particle shapes. In this study, we examined the dynamic settling progress of irregularly shaped particles by using a modified LBM-DEM model developed by Galindo-Torres [26]. An important feature of this model is its ability to efficiently and accurately solve the interaction between fluid and particles of general shapes, even non-convex ones. To the authors' knowledge, this work is the first three dimensional, direct simulation of settling of irregularly shaped particles.

This paper is organized as follows: Sec. II describes the methodology, including how to couple the Lattice Boltzmann Method with the Discrete Element Method, as well as the turbulence module. Sec. III briefly introduces various shape factors, which have been used to characterise irregularly shaped particles. Comparisons between numerical results from this study and previous ones for regularly shaped particles are presented in Sec. IV. Sec. V is focused on the settling of irregularly shaped particles, including both steady and unsteady motions. Finally Sec. VI presents conclusions from the present work.

II. METHODOLOGY

A. Lattice Boltzmann method with a turbulence module

The fluid flow is simulated by the Lattice Boltzmann equation (LBE) a discretized form of the Boltzmann equation [27]. The D3Q15 model is used with the space divided into cubic lattices. The velocity domain is discretized to fifteen velocity vectors as shown in Figure 1. The discrete velocity vectors are defined as follows:

$$\vec{e}_i = \begin{cases} 0, & i = 0, \\ (\pm1,0,0),(0,\pm1,0),(0,0,\pm1), & i = 1 \text{ to } 6, \\ (\pm1,\pm1,\pm1), & i = 7 \text{ to } 14, \end{cases}$$

Based on the Chapman-Enskog expansion of the Boltzmann equation, an evolution rule is applied to every distribution function [28]:

$$f_i(\vec{x} + \vec{e}_i\delta t, t + \delta t) = f_i(\vec{x}, t) + \Omega_{col}, \qquad (4)$$

where f_i is the probability distribution function, $\vec{x}$ is the position of the local lattice, δt is the time step and Ω_{col} is

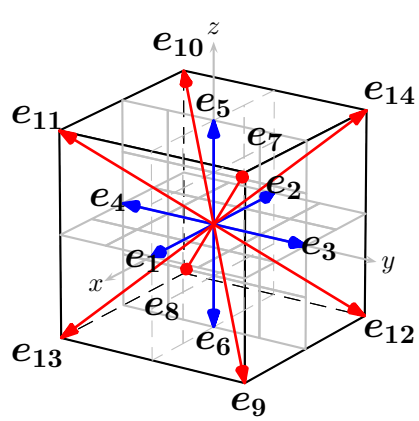

FIG. 1. Discrete velocity vectors for D3Q15 [26].

the collision operator. The well-known Bhatnagar-Gross-Krook (BGK) collision operator is used in this study,

$$\Omega_{col} = \frac{\delta t}{\tau}(f_i^{eq} - f_i), \tag{5}$$

where τ is the relaxation time and f_i^{eq} is the equilibrium distribution given by,

$$f_i^{eq} = \omega_i \rho \left(1 + 3\frac{\overrightarrow{e}_i \cdot \overrightarrow{u}}{C^2} + \frac{9(\overrightarrow{e}_i \cdot \overrightarrow{u})^2}{2C^4} - \frac{3u^2}{2C^2}\right), \tag{6}$$

with $C = \delta x/\delta t$ being the characteristic lattice velocity (δx is the lattice size). The weights are $\omega_0 = 2/9$, $\omega_i = 1/9$ for i =1 to 6, $\omega_i = 1/72$ for i =7 to 14. The kinetic viscosity is related to the relaxation time by

$$\nu = \frac{\delta_x^2}{3\delta_t}\left(\tau - \frac{1}{2}\right), \tag{7}$$

Here the Mach number is defined as the ratio of the maximum velocity to C. When $Ma \ll 1$, the LBE can be recovered to the Navier-Stokes equation. More detail can be found in [28]. The macroscopic properties of fluid such as density ρ and flow velocity $\overrightarrow{u}$ can be determined by the zero-th and the first order moment of the distribution function:

$$\begin{aligned} \rho(\overrightarrow{x}) &= \textstyle\sum_{i=0}^{14} f_i(\overrightarrow{x}), \\ \overrightarrow{u}(\overrightarrow{x}) &= \tfrac{1}{\rho(\overrightarrow{x})} \textstyle\sum_{i=0}^{14} f_i(\overrightarrow{x})\overrightarrow{e}_i, \end{aligned} \tag{8}$$

It is well known that the stability of the LBM simulation is affected by the relaxation time τ. The value of τ should not be too close to 0.5 because of the use of a linearized BGK collision operator [26]. Due to this limitation, the standard Lattice Boltzmann method is only suitable for flow at relatively low Reynolds numbers. At high Reynolds numbers, it is necessary to incorporate a turbulence module into the Lattice Boltzmann equation (LBE). In this study, the Smagorinsky subgrid turbulence module introduced by Feng [29] is employed. The scales are divided into filtered and unresolved scales by the filtering of the LBE based on the lattice size δx. The LBE can be directly solved for filtered scales. An additional relaxation time τ_a is used to represent the effect of motion at the unresolved scales [30]:

$$\tau_{total} = \tau + \tau_a, \tag{9}$$

where τ_{total} is the total relaxation time. τ_a is related to the turbulence viscosity ν_a:

$$\tau_a = \frac{3\delta_t}{\delta_x^2}\nu_a, \tag{10}$$

with the turbulence viscosity ν_a given by

$$\nu_a = (Sc\delta x)^2 \hat{S}, \tag{11}$$

where Sc is the Smagorinsky constant with a typical value range between 0.1 and 0.2; and the magnitude of the filtered strain-rate tensor $\hat{S}$ can be obtained from $\tilde{Q}_{ij}$ - the second moment of the distribution function, i.e.,

$$\hat{S} = \frac{\sqrt{2\sum_{i,j}\tilde{Q}_{ij}\tilde{Q}_{ij}}}{2\rho Sc\tau_{total}}, \tag{12}$$

with $\tilde{Q}_{ij}$ given by

$$\tilde{Q}_{ij} = \sum_{k=0}^{14} e_{ki}e_{kj}(f_k - f_k^{eq}), \tag{13}$$

where f_k and f_k^{eq} are the non-equilibrium distribution function and equilibrium distribution function, respectively.

B. Coupling approach for LBM and DEM particles

A coupling method for LBM and DEM was introduced by Owen [21] for spheres. The immersed boundary method [31] is adopted to model the interaction between fluid and solid. The LBE is modified as:

$$\begin{aligned} f_i(\overrightarrow{x} + \overrightarrow{e}_i\delta t, t + \delta t) =& f_i(\overrightarrow{x}, t) + B_n\Omega_i^s \\ &+ (1 - B_n)\left[\frac{\delta t}{\tau}(f_i^{eq} - f_i)\right], \end{aligned} \tag{14}$$

where B_n is a weighting function depending on the volume occupation fraction ε_n. Ω_i^s is an additional collision term that accounts for the momentum exchange between fluid and moving DEM particles. The bounce-back rule is applied to the interface of fluid and solid. The form of Ω_i^s proposed by Nobel [32] is used in this study:

$$\begin{aligned} \Omega_i^s =& \left[f_{i'}(\overrightarrow{x}, t) - f_{i'}^{eq}(\rho, \overrightarrow{v}_p)\right] \\ &- \left[f_i^{eq}(\rho, \overrightarrow{v}_p)f_{i'} - f_i(\overrightarrow{x}, t)\right], \end{aligned} \tag{15}$$

where the symbol i' denotes the direction opposing the i direction, and $\overrightarrow{v}_p$ is the velocity of the DEM particle at position x computed as:

$$\overrightarrow{v}_p = \overrightarrow{\omega} \times (\overrightarrow{x} - \overrightarrow{x}_c) + \overrightarrow{v}_c, \tag{16}$$

where $\overrightarrow{v}_c$ and $\overrightarrow{\omega}$ are the translational velocity and angular velocity at the DEM particle's centroid, respectively. Several forms of the weight function B_n have been discussed in [29] and [32]; however, the differences of these forms do not significantly affect the simulation results. In this study, we apply B_n as given by [32]:

$$B_n(\varepsilon) = \frac{\varepsilon_n(\tau - 1/2)}{(1 - \varepsilon_n) + (\tau - 1/2)}, \tag{17}$$

The volume occupation fraction (ε_n) plays an important role in the fluid-particles interaction. Three schemes of

ε_n have been investigated in literatures [17, 21]: an exact closed-form solution, cell decomposition and polygonal approximations. Compared with the third one, the first two schemes provide more accurate predictions [17]. However, their computational costs are high. The polygonal approximation is the most efficient scheme but only provides adequate accuracy for spheres and the ε_n value for irregularly shaped particles may deviate greatly from the exact value.

To resolve this problem, Galindo-Torres extended Owen's method by using the sphero-polyhedron technique [33–35]. A sphero-polyhedra is constructed following two steps as shown in Figure 2: first, an original polyhedra is eroded by a distance of sphero-radius R; after that, the eroded polyhedra is dilated by a sphere of the same radius (R). The so-created sphero-polyhedra are similar to the original ones but with rounded edges and corners. Therefore, the interaction between the sphero-polyhedra and LBM cells is smooth as in the case of spheres. The volume occupation fraction ε_n can then be calculated by an approximation method based on the length of an edge occupied by solid particles, i.e.,

$$\varepsilon_n = \frac{\sum_{e=1}^{12} l_e}{12\delta_x}, \tag{18}$$

where l_e is the length of the e-th edge occupied by solid particles. More details can be found in [26], where the equation was tested and demonstrated to perform as well as other existing, most accurate methods for calculating ε_n.

The total hydrodynamic force and torque over a particle covered by n cells can be calculated as:

$$\overrightarrow{F} = \frac{\delta_x^3}{\delta_t} \sum_n B_n \Big(\sum_i \Omega_i^s \overrightarrow{e_i} \Big), \tag{19}$$

$$\overrightarrow{T} = \frac{\delta_x^3}{\delta_t} \sum_n \Big[(\overrightarrow{x} - \overrightarrow{x}_c) \times B_n \Big(\sum_i \Omega_i^s \overrightarrow{e_i} \Big) \Big], \tag{20}$$

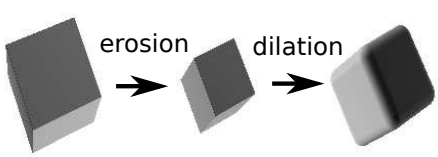

FIG. 2. A 3D sphero-cube: initially the cube is eroded or shrunk by a distance equal to the sphere radius, and then is dilated by the same sphere. After this morphological transformation, the cube ends up having rounded corners [26] .

.

III. SHAPE FACTORS

The characteristics of general particle shapes can be described by a number of shape factors. Five shape factors are considered in this work, namely: sphericity ϕ, nominal diameter d_n, surface-equivalent-sphere diameter d_A, circularity of the projected surface c and Corey shape factor CSF.

The sphericity (ϕ) has been suggested as an appropriate single shape factor for isometric non-sphere particles [1, 2] and is defined as follows [36]:

$$\phi = \frac{S_{sphere}}{S} \tag{21}$$

with S_{sphere} being the surface area of volume-equivalent-sphere and S is the surface area of the particle.

However, measurement of the particles surface area is difficult in practice, especially for particles of irregular shapes.

A widely used shape factor is the nominal diameter d_n defined as the diameter of the volume-equivalent-sphere [36]. Another widely used diameter is the surface-equivalent-sphere diameter,

$$d_A = \sqrt{\frac{4A_p}{\pi}} \tag{22}$$

where A_p is the projected area of the particle.

The circularity of the projected area has also been examined [1] which is given by:

$$c = \frac{\pi d_A}{P_p} \tag{23}$$

where P_p is the perimeter of the particles projected area.

The Corey shape factor CSF [37] is directly related to the sizes of the particle in three dimensions, as defined by:

$$CSF = \frac{d_s}{\sqrt{d_i d_l}} \tag{24}$$

where d_l, d_i and d_s are the longest, intermediate, and shortest particle axes lengths, respectively.

IV. VALIDATION

A. Settling of sphere

The settling of a sphere in a viscous fluid is simulated to examine the dynamic behaviour of the sphere and associated fluid motion. The domain size is $6.6d_n \times 6.6d_n \times 10.6d_n$. Ladd [23] suggested that the sphere's diameter d_n should be larger than 9 LBM cells to ensure a sufficient accuracy, and here we set $d_n = 30$ LBM cells size, which is equal to 15 mm in the physical unit. The sphere is placed at a height of $8d_n$ from the bottom. The particle's density ρ_s is 1120 kg/m^3; the fluid density ρ_f and

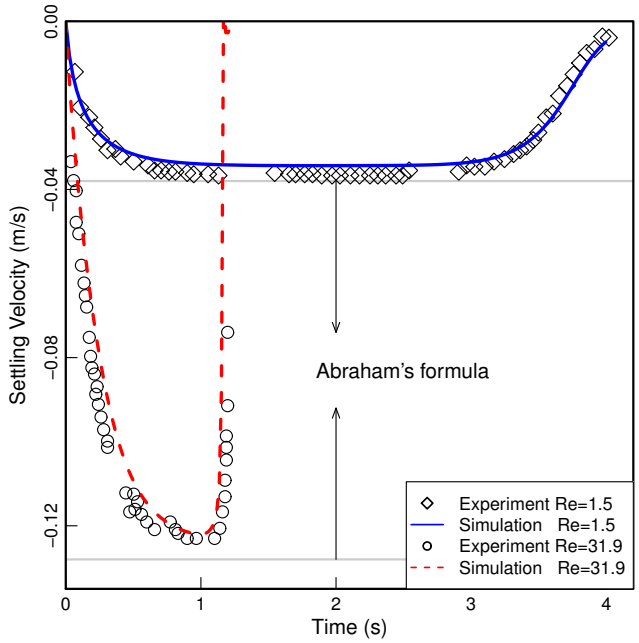

FIG. 3. Comparison between simulated settling velocities and experimental measurements for sphere particles during the settling process.

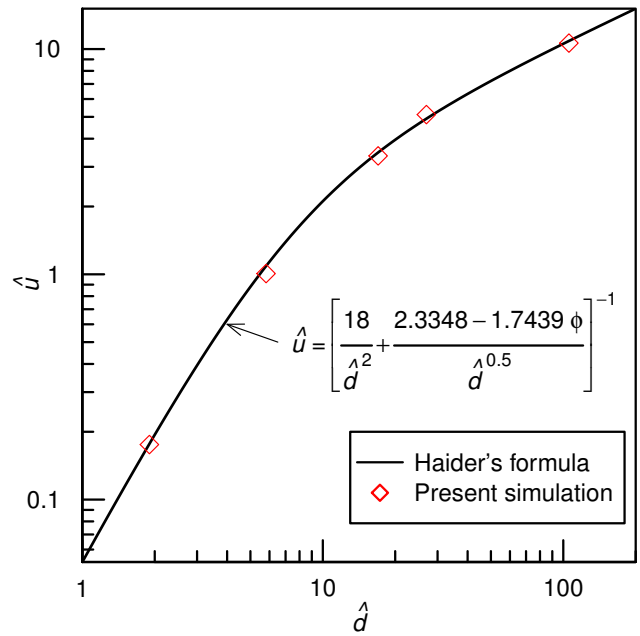

FIG. 4. Comparison between our simulation settling velocity and experiments for the sphere.

the kinetic viscosity ν are set according to [12]. The values of all the parameters used in the simulations are listed in Table I. Wall boundary conditions are applied at the boundaries. Note that in the simulations, the gravity is only applied to the DEM particle and thus a relative gravity given by $(1-\rho_f/\rho_s)g$ is used as suggested by Feng [20].

The time series of simulated settling velocities are compared to the experimental data presented in [12] for $Re = 1.5$ and $Re = 31.9$ as shown in Figure 3. Also plotted in the figure are predicted terminal settling velocities based on an empirical drag coefficient formula from [38]:

$$C_D = \frac{24}{(9.06)^2}\left(\frac{9.06}{\sqrt{Re}}+1\right)^2, \tag{25}$$

TABLE I. Parameter values used in and calculated from the simulations in comparison with experimental data. u_s/u_e is the ratio of simulated terminal settling velocity to measured value from physical experiments.

Re [−]	St [−]	ρ_f [kg/m^3]	ν [m^2/s]	u_s/u_e [−]
1.5	0.19	970	0.385	0.950
4.1	0.53	965	0.220	0.972
11.6	1.50	962	0.117	0.945
31.9	4.13	960	0.060	0.951

Overall the simulation results agree well with both the experimental data and predictions of Eq. 25. The maximum velocities in both the simulation and experiment are of slightly lower magnitudes than those predicted by Eq. 25 because of the hindrance effect of the wall boundaries: particle motion affected by the additional resistance due to the container walls. The ratio of simulated terminal settling velocities to measured values from the experiment(u_s/u_e) is around 0.95 as given in Table I. Similar results have been reported by [21, 26]. The model slightly over-predicts C_D when Re is less than 40. This may linked to the form of the weighting function B_n used.

B. Settling of cube

Another simulation is performed for a cube of 20 LBM cells (i.e., $d_n = 20$ LBM cells size) with a sphero-radius of 1 LBM cell size. The depth and width of the domain are both $5d_n$ but the height increases with the Reynolds number from $16d_n$ to $72d_n$. Re varies over the range from 1 to 1200; for $Re > 100$, the cube always tends to rotate during the settling process and thus the average terminal velocity is used for comparison. A previous study by Haider[2] has developed a quantitative relation between the dimensionless diameter $\hat{d}$ and the dimensionless terminal velocity $\hat{u}$ for non-spherical particles based on experimental data:

$$\hat{u} = \left[\frac{18}{\hat{d}^2} + \frac{2.3348 - 1.7439\phi}{\hat{d}^{0.5}}\right]^{-1} \tag{26}$$

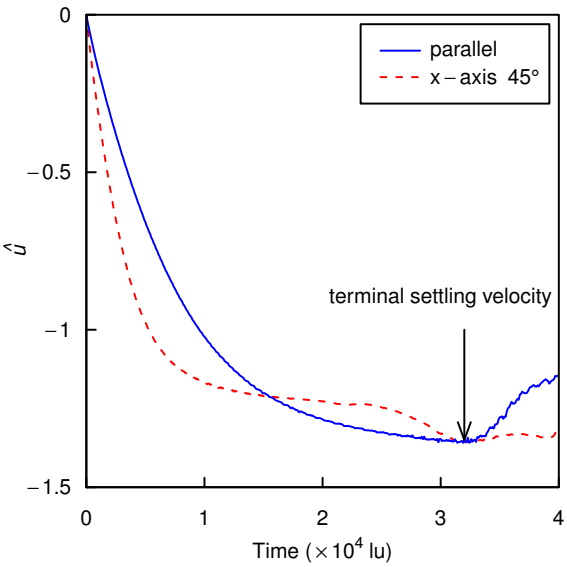

FIG. 5. Comparison of settling velocity between cubes released with different initial orientations: the edges of the cube parallel to the container (blue solid line), and with a rotation of 45° around the x axis (red dotted line). The viscosity $\nu = 2.0 \times 10^{-5}\mathrm{m}^2/\mathrm{s}$. The variations shown toward the end of the simulation are due to the effect of the lower boundary.

where ϕ is the sphericity of the particle and

$$\hat{d} = d_n \left[\frac{g(\rho_s - \rho_f)}{\nu^2 \rho_f^2} \right]^{\frac{1}{3}} \tag{27}$$

and

$$\hat{u} = u_p \left[\frac{\rho_f}{g\nu(\rho_s - \rho_f)} \right]^{\frac{1}{3}} \tag{28}$$

Figure 4 shows an excellent agreement between the results of this study and Haider's predictions with the maximum difference of $\hat{u}$ lower than 3%. To determine the influence of the particle's initial orientation, a series of simulations are performed with different rotations of the cube. Although these simulations show different settling patterns at the beginning, the settling of the cube in all cases reaches the steady state with the same value of terminal velocity for a given Re (see Figure 5).

V. SETTLING OF IRREGULAR SHAPED PARTICLES

The irregularly shaped particles used in this study are described by 3D polygon meshes. The advantages of these meshes for the study are two-fold: firstly, they can be used to describe bodies of any shapes with a sufficient resolution; and secondly, compared with the method of using a cluster of spheres to approximate general particle shapes, using a mesh can avoid flow passing through the inside of particles since there is no void space within the solid body. Seven particles with different geometrical shapes are constructed as shown in Figure 6. The mesh information and the shape factors of all the particles are summarised in Table. II. Depending on the complexity of the particle shape, the mesh size is varied to ensure enough resolution. All particles have the same volumetric mass density and the same volume of an equivalent sphere of diameter $d_n = 13$ lattice unit. Thus the gravity force is the same for all the particles and hence the only difference between these particles is their shapes. The sphericity, circularity and Corey shape factor of the particles vary from 0.5 to 1. The Re is controlled by changing the viscosity. Four values of kinematic viscosity ν are applied in the simulation: 2.0×10^{-4}, 1.0×10^{-4},

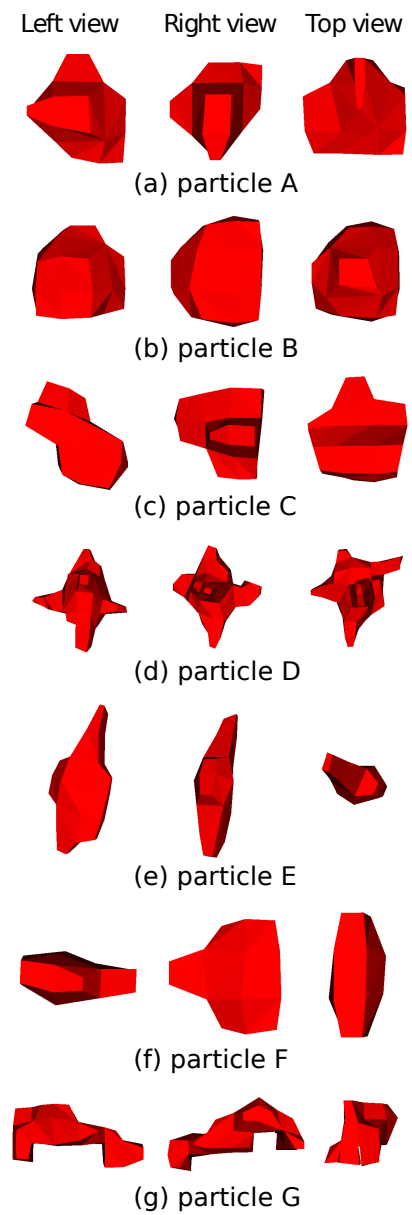

FIG. 6. Three views of the irregularly shaped particles investigated.

TABLE II. Mesh information and shape factors of particles.

Particle	Vertices	Edges	Faces	Sphericity ϕ	d_A/d_n	Circularity c	Corey factor Co
A	40	114	76	0.8215	1.3254	0.9204	0.797
B	46	132	88	0.9037	1.2577	0.9526	0.939
C	47	95	100	0.5923	1.4784	0.9009	0.875
D	96	290	196	0.6268	1.4148	0.7418	0.840
E	42	120	80	0.7083	1.5611	0.7485	0.446
F	28	78	52	0.7763	1.4875	0.8772	0.440
G	59	173	116	0.5352	1.5635	0.6182	0.667

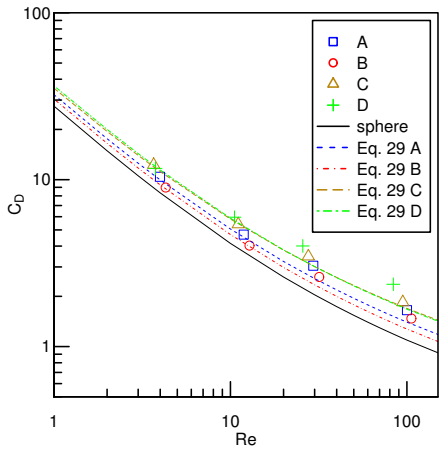

(a)Group 1

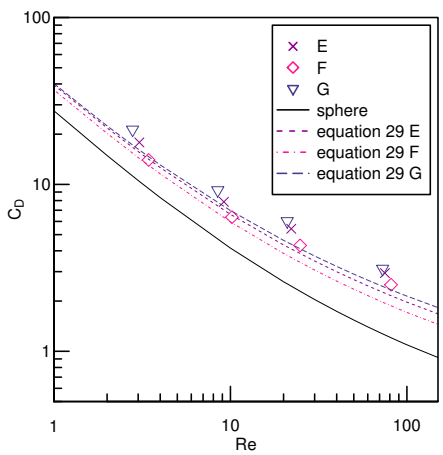

(b)Group 2

FIG. 7. Drag coefficient of irregularly shaped particles as a function of the Reynolds number.

5.0×10^{-5}, $2.0 \times 10^{-5}\mathrm{m}^2/\mathrm{s}$.

An experimental work has been presented by Tran-Cong et al [1], who studied the drag coefficient of irregularly shaped particles. Based on the experimental results, they modified the drag coefficient formula of Clift et al [3] to incorporate the shape effect:

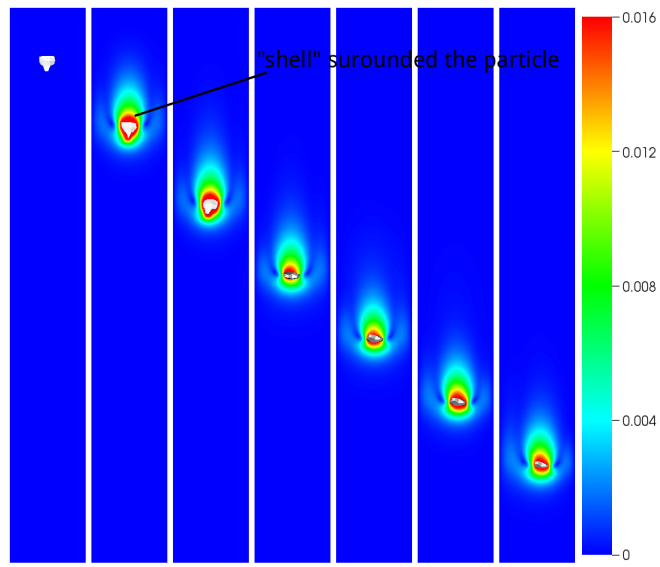

FIG. 8. Cross sectional contour plot of fluid velocity field for particle F at $Re = 3.04$. The colourmap shows the magnitude of the fluid velocity.

$$C_D = \frac{24}{Re}\frac{d_A}{d_n}\left[1 + \frac{0.15}{\sqrt{c}}\left(\frac{d_A}{d_n}Re\right)^{0.687}\right] + \frac{0.42\left(\frac{d_A}{d_n}\right)^2}{\sqrt{c}\left[1 + 4.25\times 10^4\left(\frac{d_A}{d_n}Re\right)^{-1.16}\right]}, \quad (29)$$

The drag coefficient C_D simulated in this study and the results from Eq. 29 versus Re are plotted in Figure 7. For comparison, the predictions for a volume-equivalent sphere are also included. The particles are divided into two groups based on whether their Corey factors (CSF) are greater than 0.7 or not since different patterns of settling are observed for these two groups of particles in this study. For group 1, C_D based on the simulation results agrees well with Eq. 29 in the low range of Re; however when $Re > 20$, the simulated values are slightly higher and the difference increases with Re. Tran-Song

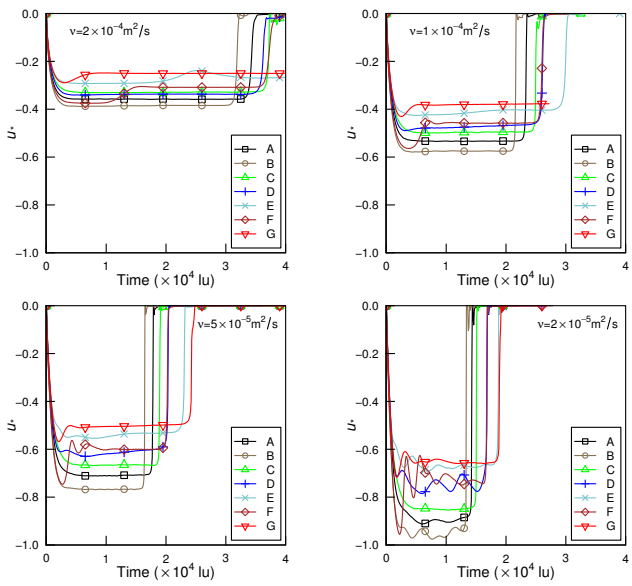

FIG. 9. Time series of dimensionless settling velocities of irregularly shaped particles simulated with different viscosity values.

et al. [1] suggested that Eq. 29 is suitable in the range of $Re < 50$ for tetrahedrons and $Re < 200$ for cubes. C_D should approach a constant when Re is close to Newton's regime which the settling behaviour is dominated by vortices behind the particle. Also at high Re, the settling behaviour may be affected by the wall boundary condition; and this effect can be reduced by increasing the simulation domain size, which however would lengthen the simulation time. Note that a periodic boundary condition is not suitable at high Re, because of the wake left behind the particle [19]. Compare with group 1, the deviation of the simulation results for group two particles from Eq. 29 cannot be ignored even at low Re. C_D for all 7 irregularly shaped particles are higher than that for the sphere. The highest C_D is observed for particle G, which has the lowest sphericity and circularity but highest d_A/d_n. In contrast, particle B with the highest sphericity circularity and lowest d_A/d_n has the smallest value of C_D.

For a given Re, C_D for both group 1 and group 2 particles increases with d_A/d_n, consistent with the predictions of Eq. 29. Figure 8 shows images of the flow field and the motion of particle F for $\nu = 2.0 \times 10^{-4}\mathrm{m}^2/\mathrm{s}$. At the beginning, the plane of the particle's maximum projected area is parallel with the direction of the settling motion (maximum projection indicated by the white colour in the first sub-figure on the left hand side); then the particle starts rotating until the maximum cross-section becomes normal to the direction of motion (minimum projection on the plane parallel to the settling direction shown in the last sub-figure on the right hand side).

Figure 9 shows the time series of settling velocities simulated with different viscosity values. The settling velocities are normalized as $u_* = u_p \left[(\frac{\rho_s}{\rho_f} - 1) g d_n \right]^{-\frac{1}{2}}$ [39]. The results show that the terminal velocity increases with decreasing viscosity as expected. The settling dynamics of the particles depend largely on Re. At low Re, the settling of all particles reaches a terminal velocity under the balance of drag and gravity forces after an initial acceleration stage. Two different types of u_* behaviours can be observed: firstly an 'accelerating' behaviour for group 1 with u_* rapidly increasing initially but gradually approaching a steady state and reaching the terminal velocity; secondly an 'accelerating-decelerating' behaviour for group 2. The second behaviour is characterised by an overshoot of the settling velocity particles accelerated with u_* reaching a maximum value that exceeds the terminal velocity and then decelerated to the steady state condition given by the terminal velocity. The difference may be linked to the ratio of the minimum projected area to the maximum projected area (related to CSF), which is considerably lower than 1 (< 0.7) for group 2 particles. For these particles, the drag force as a function of the projected area would be relatively small, permitting the over-acceleration of particles.

Previous experimental results indicate that there is no steady-state settling for irregularly shaped particles when Re is higher than 100, unless they are released with the maximum cross-section normal to the vertical axis in the settling direction [1, 13, 14]. These particles tend to show a spiral trajectory at high Re as they rotate around a horizontal axis. The same phenomenon is observed in the present simulations. Except for particle C, the settling velocity of all particles fluctuates with time but around a constant value. The terminal velocity increases with decreasing viscosity. The motion of particles is strongly affected by the horizontal force, different from the low Re case where the horizontal force is very weak. The exceptional behaviour of particle C will be discussed in the following section.

From Eq. 3 it can be seen that the projected area plays an important role in the settling process. Figure 10 shows the x, y, and z component of the angular velocity, i.e., ω_x, ω_y and ω_z as well as the dimensionless projected area P_A for particle B, C, E and F. The dimensionless projected area P_A is define as the ratio of the projected area to πd_n^2 (projected area of a volume-equivalent sphere). In all the cases, P_A increases at the beginning, which means that all the particles tend to adjust their orientations until the maximum cross-section becomes normal to the settling direction. At low Re, P_A for most of the particles reaches a constant after the acceleration stage. However, Figure 10(b) and Figure 10(c) shows that even after reaching the steady state, P_A still changes with time. This suggests that minor changes of the projected area may persist but do not strongly affect the settling velocity at low Re. Because the particle moves with a layer of water around it (Figure 8), if the thickness of the 'water shell' is large enough, the settling velocity is not sensitive to the rotation. The x and y component of the angular

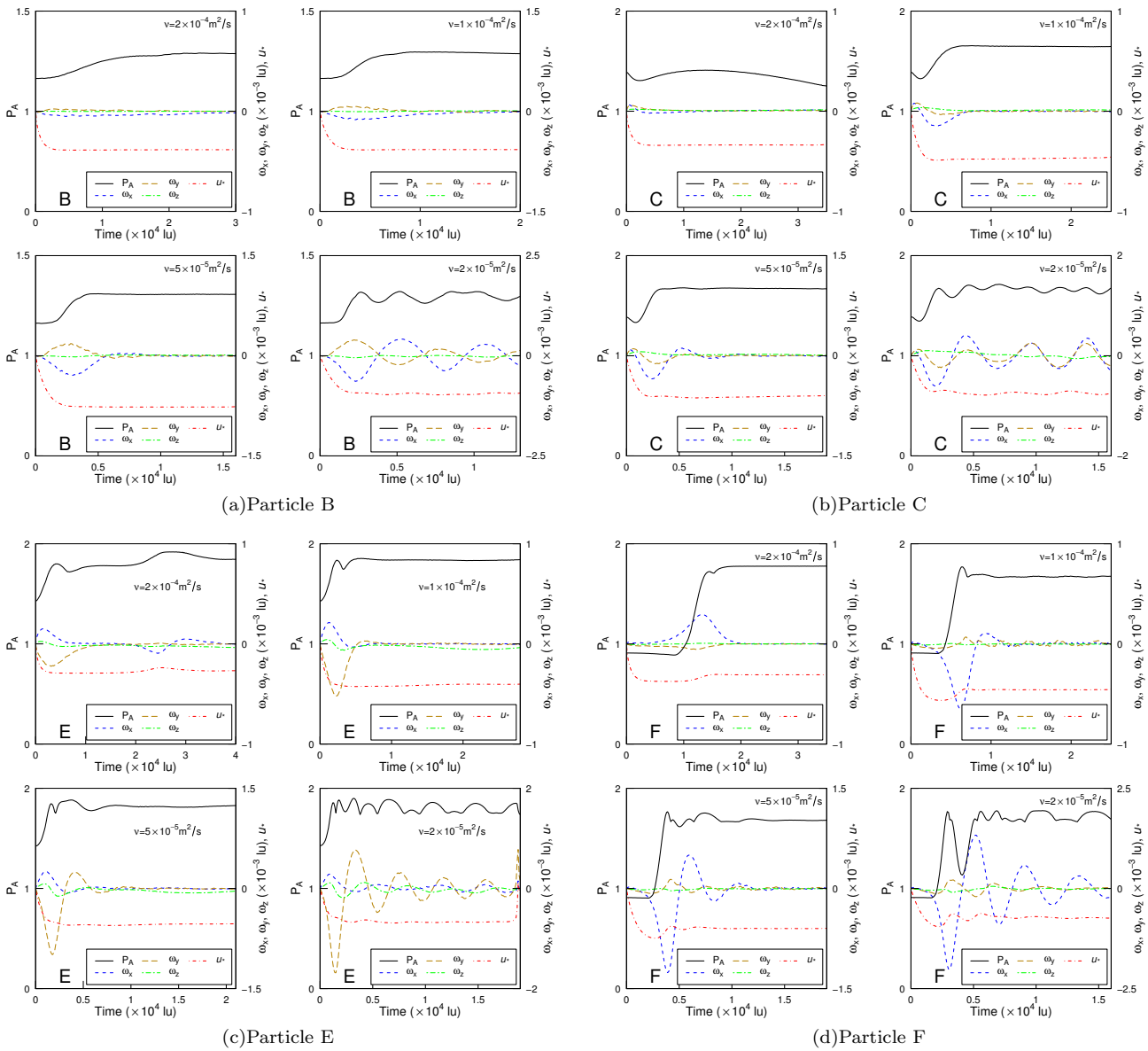

FIG. 10. Time series of projected area and angular velocities of particle B, C, E and F simulated with different viscosity values.

velocity (ω_x and ω_y) also increase at the beginning but subsequently become very small, approaching zero. At high Re, ω_x and ω_y as well as P_A show periodic fluctuations. The transition from the steady state behaviour for low Re to this oscillating condition appears to occur when Re is approximately equal to 100. The amplitudes of the oscillations of ω_x and ω_y depend on Re. For the z component of the angular velocity ω_z, the value is always near zero for all Re.

As shown in Figure 10(a) and Figure 10(b), the amplitudes of ω_x and ω_y are of the same order of magnitude for particles B and C. However, ω_x and ω_y differ significantly for particles E and F (Figure 10(c) and Figure 10(d)). There appears to be a major rotating axis, either x or y, for these particles with low CSF. Although the amplitude of the larger component between ω_x and ω_y decreases with time, its value does not reach zero, as confirmed by additional simulations. A detailed discussion of this persistent rotation is given in the next section. The streamlines for particle A in cases with different Re are plotted in Figure 11. The results show that vortexes form and move away from the particle surface at high Re. These vortexes are directly linked to the unsteady behaviour of particles.

As mentioned above, the irregularly particles will approach an unsteady (oscillating) state when Re exceeds 100. To investigate the unsteady behaviour of particles, additional simulations with an increased height of the domain are performed for $\nu = 2.0 \times 10^{-5}$ and $1.0 \times 10^{-5}\mathrm{m}^2/\mathrm{s}$, which correspond to Re of approximately

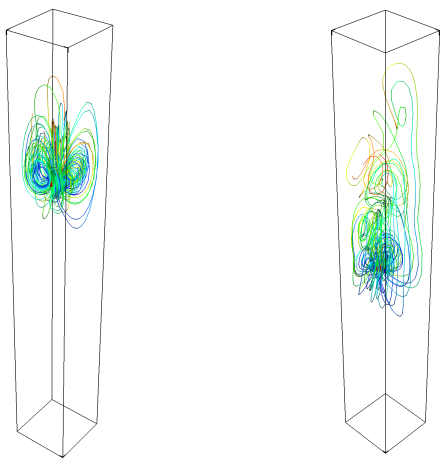

(a)$\nu = 2.0 \times 10^{-4}\mathrm{m}^2/\mathrm{s}$ (b)$\nu = 2.0 \times 10^{-5}\mathrm{m}^2/\mathrm{s}$

FIG. 11. Streamlines of particle A simulated with two viscosity values: the seeds of streamlines are set around the particle and with equal spacing between each other.

100 and 200, respectively. Figure 12 shows clearly the periodic oscillations of the angular velocity around zero. As P_A is directly controlled by the angular velocity, it also fluctuates around a mean value after undergoing a relatively rapid increase at the beginning. The amplitudes of ω_x and ω_y increase with Re; however, the oscillation frequency is not sensitive to Re. When the particles move close to the bottom in the case with $Re = 200$, two different trends of the angular velocity are found: for particle B and E, the amplitudes of ω_x and ω_y tend to decrease, while the opposite occur for particle C and F. The cause of the different trends requires further investigation.

In a previous experimental study, the dynamical behaviours of thin disks were characterised as being 'steady', 'periodic' and 'chaotic' or 'tumbling'. These behaviours depend on the moment of disk inertia and Re [13]. In the present study, we observe 'steady' and 'periodic' behaviours of irregularly shaped particles within the range of Re examined. Figure 13 shows the phase diagram. It should be pointed out that for thin disks only one moment of inertia is necessary because the normal one I_n can be ignored. For the case of particles of general shapes, the moment of inertia $\mathbf{I}$ should be considered as a tensor. Moreover, $\mathbf{I}$ is not a constant in the static Cartesian coordinates during settling and thus the eigenvalues (I_i) of the tensor are used to characterize the unsteady behaviour of particles. We note that the transition between 'steady' and 'periodic' behaviours occurs in the range of $80 < Re < 300$ and the critical Re is a function of $\mathbf{I}$. A boundary separating the two behaviours may be found only on the phase diagram based on the maximum eigenvalue I_{max} and Re. It is interesting that the curve of this boundary appears to have a similar geometric feature to that for thin disks. The overlap for the medium and minimum eigenvalues (I_{mid} and I_{min}) implies that I_{max} play the major role. One may note that the moment of inertia used in [13] is I_{min}; however I_{max} would have given the same results as $I_{max} = 2I_{min}$ for thin disks.

VI. CONCLUDING REMARKS

We have investigated the settling dynamics of single particles of complex, irregular shapes in a still fluid through simulations using a coupled Discrete Element-Lattice Boltzmann model. This model was first validated with experimental results for spheres conducted by Cate et al.[12] and for cubes carried out by Haider[2] under conditions of moderate Reynolds numbers. Seven irregularly shaped particles were constructed using 3D polygonal meshes with the same volume. The simulated settling velocity and drag coefficient for these particles were found to be in a reasonably good agreement with predictions by the formula of Tran-Cong et al. [1] for particles with $CSF < 0.7$ at $Re < 20$. However, the simulation results deviated significantly from the predictions of the existing formula as Re increases beyond 20.

The particle shapes not only affect the terminal settling velocity, but also the dynamic settling process. When Re is lower than 100, the settling of the particles reaches a steady-state through different transient processes depending on the particle shape. Particles of shapes with Corey factors larger than 0.7 get accelerated to the terminal velocity. Particles of shapes with Corey factors less than 0.7 go through an accelerating-decelerating with u_* increased to a maximum settling velocity exceeding the terminal velocity and subsequently decreased back to the terminal velocity.

When Re is higher than 100, the time series of the particle angular velocities and projected areas show a periodically oscillating behaviour for all the seven particles. The component of angular velocity normal to the settling direction was found to be unimportant as it does not affect the projected area. The simulation results showed that the oscillation amplitude of the particle angular velocity in the transverse directions increases with Re; however the frequency of the oscillation is not sensitive to Re.

The transition between 'steady' and 'periodically oscillating' behaviours of the simulated irregularly shaped particles depends on a critical Re, consistent with previous research findings [1, 16]. However, this study showed that the dynamic behaviours of irregularly shaped particles are also related to the inertia tensor $\mathbf{I}$. In particular, the maximum eigenvalue of the inertia tensor (I_{max}) appears to play a major role in determining the steady or periodically oscillating behaviour of particles.

The present study has shown important effects of irregular shapes on the settling dynamics of particles. Future studies are required to examine how dimensionless parameters such as Re and C_D can be combined with shape factors to develop a unified theoretical framework for quantifying the behaviours of particles of general shapes.

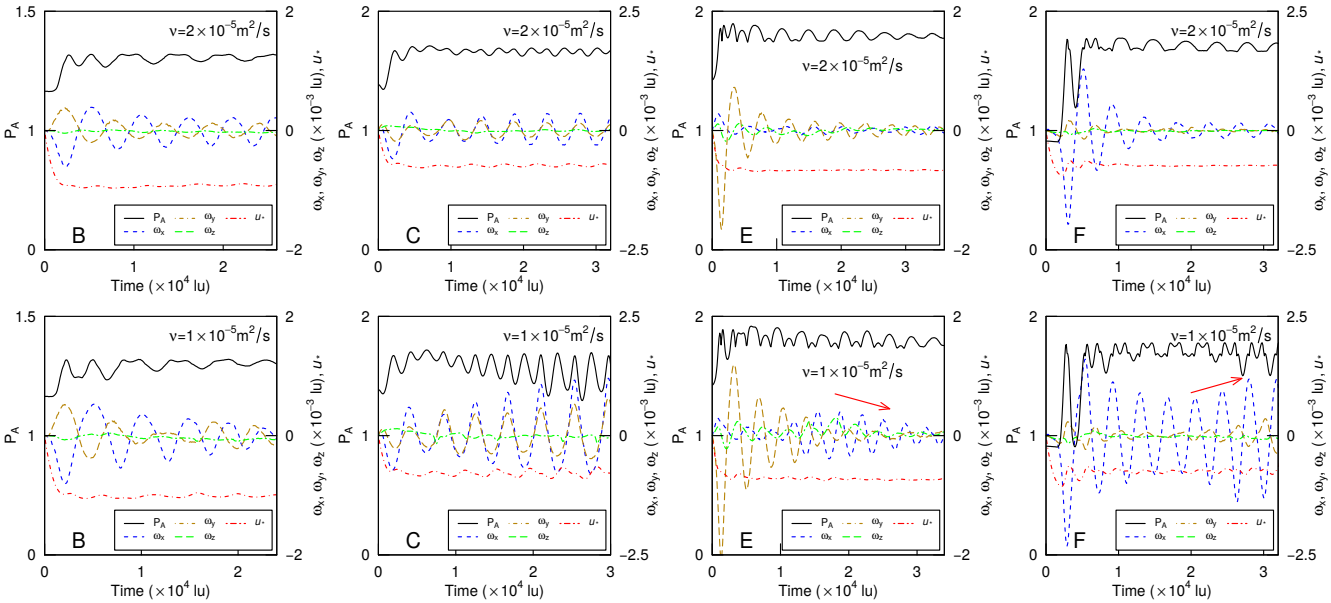

FIG. 12. Time series of projected areas and angular velocities of particle B, C, E and F simulated with different viscosity values and an increased height of the domain.

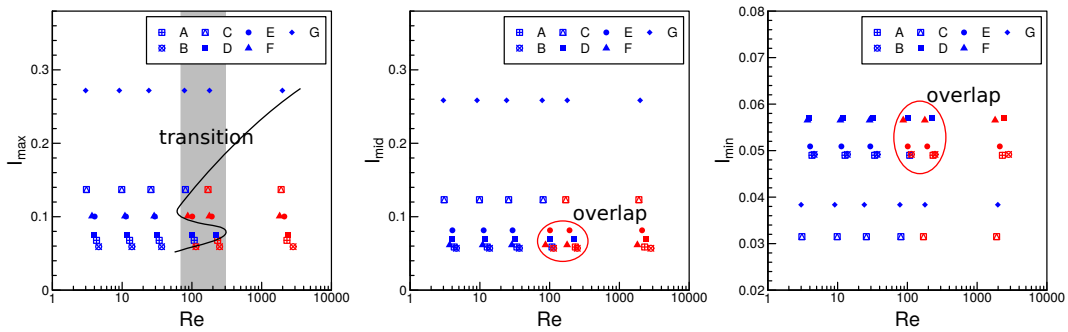

FIG. 13. Phase diagram: the settling behaviour of irregularly particles as a function of Reynolds number Re and maximum inertia I_{max}.

The Discrete Element and Lattice Boltzmann Method again can offer an effective simulation approach to produce data for elucidating the form of these dimensionless parameters and their relationships.

ACKNOWLEDGEMENT

We gratefully acknowledge the funding from the Natural Science Foundation of China (51239003, 51125034, 51109059), the ARC Discovery project (DP140100490), the Natural Science Foundation of Jiangsu Province, China (BK2011749). Computational resources were provided by the the Macondo cluster, hosted by the School of Civil Engineering at The University of Queensland.

[1] S. Tran-Cong, M. Gay, and E. E. Michaelides, Powder Technology **139**, 21 (2004).
[2] A. Haider and O. Levenspiel, Powder technology **58**, 63 (1989).
[3] R. Clift, J. R. Grace, and M. E. Weber, *Bubbles, drops, and particles* (Courier Corporation, 2005).
[4] A. Khan and J. Richardson, Chemical Engineering Communications **62**, 135 (1987).
[5] F. M. White, "Fluid mechanics," (2003).
[6] D. Leith, Aerosol science and technology **6**, 153 (1987).
[7] G. H. Ganser, Powder Technology **77**, 143 (1993).
[8] E. Loth, Powder Technology **182**, 342 (2008).

[9] N. Clark, P. Gabriele, S. Shuker, and R. Turton, Powder technology **59**, 69 (1989).

[10] E. Pettyjohn and E. Christiansen, Chemical Engineering Progress **44**, 157 (1948).

[11] N.-S. Cheng, Journal of hydraulic engineering **123**, 149 (1997).

[12] A. Ten Cate, C. Nieuwstad, J. Derksen, and H. Van den Akker, Physics of Fluids (1994-present) **14**, 4012 (2002).

[13] S. B. Field, M. Klaus, M. Moore, and F. Nori, Nature **388**, 252 (1997).

[14] W. W. Willmarth, N. E. Hawk, and R. L. Harvey, (1964).

[15] E. Marchildon, A. Clamen, and W. Gauvin, The Canadian Journal of Chemical Engineering **42**, 178 (1964).

[16] A. Hölzer and M. Sommerfeld, Computers & Fluids **38**, 572 (2009).

[17] L. Wang, G. Zhou, X. Wang, Q. Xiong, and W. Ge, Particuology **8**, 379 (2010).

[18] R. Beetstra, M. Van der Hoef, and J. Kuipers, Computers & fluids **35**, 966 (2006).

[19] A. El Yacoubi, S. Xu, and Z. Jane Wang, Journal of Fluid Mechanics **705**, 134 (2012).

[20] Z.-G. Feng and E. E. Michaelides, Journal of Computational Physics **195**, 602 (2004).

[21] D. Owen, C. Leonardi, and Y. Feng, International Journal for Numerical Methods in Engineering **87**, 66 (2011).

[22] G. G. Stokes, *On the effect of the internal friction of fluids on the motion of pendulums*, Vol. 9 (Pitt Press, 1851).

[23] A. J. Ladd, Journal of Fluid Mechanics **271**, 285 (1994).

[24] B. K. Cook, D. R. Noble, and J. R. Williams, Engineering Computations **21**, 151 (2004).

[25] P. A. Cundall and O. D. Strack, Geotechnique **29**, 47 (1979).

[26] S. Galindo-Torres, Computer Methods in Applied Mechanics and Engineering **265**, 107 (2013).

[27] S. Galindo-Torres, A. Scheuermann, and L. Li, Physical Review E **86**, 046306 (2012).

[28] A. A. Mohamad, *Lattice Boltzmann method: fundamentals and engineering applications with computer codes* (Springer Science & Business Media, 2011).

[29] Y. Feng, K. Han, and D. Owen, International Journal for Numerical Methods in Engineering **72**, 1111 (2007).

[30] H. Yu, S. S. Girimaji, and L.-S. Luo, Journal of Computational Physics **209**, 599 (2005).

[31] R. Mittal and G. Iaccarino, Annu. Rev. Fluid Mech. **37**, 239 (2005).

[32] D. Noble and J. Torczynski, International Journal of Modern Physics C **9**, 1189 (1998).

[33] S. Galindo-Torres, D. Pedroso, D. Williams, and L. Li, Computer Physics Communications **183**, 266 (2012).

[34] S. Galindo-Torres, F. Alonso-Marroquín, Y. Wang, D. Pedroso, and J. M. Castano, Physical Review E **79**, 060301 (2009).

[35] S. Galindo-Torres and D. Pedroso, Physical Review E **81**, 061303 (2010).

[36] H. Wadell, The Journal of Geology , 310 (1933).

[37] W. E. Dietrich, Water resources research **18**, 1615 (1982).

[38] F. F. Abraham, Physics of fluids **13**, 2194 (1970).

[39] J. A. Jiménez and O. S. Madsen, Journal of waterway, port, coastal, and ocean engineering **129**, 70 (2003).